IEEE Access
Multidisciplinary | Rapid Review | Open Access Journal

Received 8 June 2023, accepted 14 August 2023, date of publication 21 August 2023, date of current version 25 August 2023.

Digital Object Identifier 10.1109/ACCESS.2023.3306779

RESEARCH ARTICLE

Measurement Simulation System of Fringe Projection Profilometry Based on Ray Tracing

QIUSHUANG ZHANG[1], MINGYI XING[2], HONGBIN LI[1], XU LI[1], AND TINGLI WANG[1]
[1]College of Electromechanical Engineering, Qingdao University of Science and Technology, Qingdao 266061, China
[2]Ultrasound Research and Development Department, Hisense Medical Equipment Company Ltd., Qingdao 266100, China

Corresponding author: Tingli Wang (verena_bit@163.com)

This work was supported by the Shandong Provincial Natural Science Foundation under Grant ZR2022QE283 and Grant ZR2021QE151.

ABSTRACT Fringe projection profilometry (FPP) plays an important role in the quality control of complex surface workpieces. Simulation using realistic image synthesis referring to physical sensors provide valid measures for the design and optimization of FPP systems. In the simulation of FPP, ray tracing can simulate the fringe image acquisition process, considering the comprehensive influence of light source, camera and object attributes. Therefore, a measurement simulation system of FPP based on ray tracing is developed in this paper. The simulation model and measurement principle of FPP are introduced. On this basis, the methodology of simulating camera imaging by ray tracing is proposed, including scene construction, ray generation and gray value calculation. Principle experiments are carried to verify the accuracy and efficiency of simulation system, and comparative experiments are conducted for demonstrating its reproducibility to physical system. The proposed system provides a convenient and accurate mean for analyzing measurement errors and optimizing inspection strategy.

INDEX TERMS Fringe projection profilometry, simulation system, ray tracing, optical measurement.

I. INTRODUCTION

Three-dimensional(3D) measurement technology plays an important role in the quality control of complex workpieces [1], [2], [3]. Higher requirements for measurement accuracy are put forward, with the development of precision machining. Fringe projection profilometry (FPP) is a widely used 3D measurement technology whose measurement accuracy is affected by coupling factors, such as sensor parameters, object properties and measurement strategies [4], [5], [6]. It is difficult to study the influence of different parameters on measurement accuracy only by experiments. Therefore, the measurement simulation system is constructed to simulate error sources, which can improve measurement accuracy, measurement strategy and sensor parameters.

Thomas Böttner et al. constructed a virtual 3D measurement system to estimate the measurement accuracy of different positions, but did not fully consider the surface information of measured object [7]. Weickmann J et al. proposed a simulation method for monocular measurement system, which considered the error factors in the phase retrieve and calibration process [8]. However, the simulation results were inaccurate for complex surfaces with obvious changes in local normal vectors. A. Weckenmann et al. developed an assistance system of FPP, but the modeling of optical system was simple [2], [9]. Peng T proposed the algorithms and models for 3-D shape measurement using digital fringe projections, which was only applicable to the monocular FPP system [10]. Yingchun et al. proposed an FPP simulation system based on inverse ray tracing to simulate the modulation process of structured light field [11]. Li et al. improved the calculation efficiency and accuracy of the above system [12]. Haskamp et al. developed a virtual measurement system based on ray tracing, but the simulation of lens defocus was not sufficient [13]. Peter lutzk et al. conducted Monte Carlo simulation of 3D measurements of transparent objects, but the calculation was complex and time-consuming [14]. Peter lutzk et al. proposed a 3D measurement system integrated hyperspectral imaging, which was an improvement in multiple data acquisition [15]. Stephan presented a simulation toolset for computer aided inspection planning of 3D laser scanner [16]. Mahsa focused on physical simulation

The associate editor coordinating the review of this manuscript and approving it for publication was Stavros Souravlas.

of laser triangulation measurement system and verified a sensor-realistic simulation framework [17]. Becker built up a virtual close range photogrammetric sensor using POV Ray, a free ray tracing software [18]. A simulation approach was used to simulate the process of photography in a 3D computer modeling environment by Mezhenin [19]. Gajic proposed a simulator for human body scanning to improve the 3D data acquisition method based on photogrammetry [20].

The above researches simulate the FPP measurement system, however, factors causing measurement errors have still not been fully considered in the simulation system. This limitation is addressed by our study, in which a measurement simulation system of FPP based on ray tracing is developed. Ray tracing is a technology used for scene rendering in computer graphics [21], [22]. Considering the factors such as light source, camera and object attributes, it is applied to the 3D measurement simulation of FPP, which can simulate the fringe pattern capturing. Our work is described in this paper, which is structured as follows. The simulation model is given in Section II. Then, the methodology where the ray tracing has been used to simulate the camera imaging process, including scene construction, ray generation and gray value calculation—is detailed in Section III. Experimental validation is described in Section IV; the discussion and our conclusions are presented in Section V and Section VI respectively.

II. SIMULATION MODEL

A. MEASUREMENT PRINCIPLE OF FRINGE PROJECTION PROFILOMETRY

The 3D measurement system of FPP is composed of cameras and projector, as shown in Figure 1. The projector projects sinusoidal phase-shift fringe pattern sequences onto object surface. At the same time, the cameras capture the fringe patterns which is modulated by the surface geometry. Full-field absolute phase of surface can be retrieved utilizing the sinusoidal fringe pitch and phase shift parameters, and then corresponding image points are searched according to geometric and phase constraints [23]. Finally, point cloud data is reconstructed by the internal and external calibration parameters of binocular cameras.

According to the measurement principle, the fringe patterns are preconditions of reconstructing point cloud. The imaging process can be described as that cameras sample and quantify the light intensity reflected by object surface to produce gray images. The measurement simulation system aims to simulate the fringe projection and image capturing. The difference from physical measurement system is reflected in two aspects: the measured object is a geometric model; and the output image is generated by calculation, rather than through the complex optical system.

B. OVERALL SCHEME OF SIMULATION SYSTEM

The measurement simulation system of FPP based on ray tracing realizes the accurate simulation of three physical processes: fringe projection, surface reflection and image capturing. The output is the fringe pattern modulated by the surface geometry. As shown in Figure 2, firstly, modeling parameters of measurement scene are determined, including sensor parameters, calibration parameters, phase-shift fringes, CAD model and reflectance characteristics. Then, the simulated measurement scene is constructed, and the graphics processing unit (GPU) is used to execute the ray tracing algorithm to generate rays and intersect with the object in parallel. On this basis, the gray value of the image is solved to render the fringe pattern. Finally, the point cloud of object is obtained through data processing.

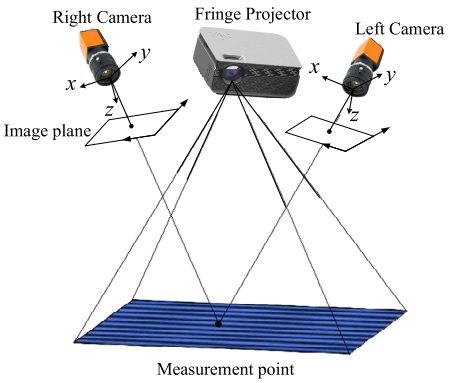

FIGURE 1. 3D measurement system of FPP.

III. METHODOLOGY

Considering the complexity of the measurement system and object surface, it is difficult to get the light intensity distribution on the image plane by analytical method. Therefore, the ray tracing is used to simulate the camera imaging process. The principle of ray tracing is to estimate the light intensity by sampling, specifically including scene construction, ray generation and gray value calculation

A. SCENE CONSTRUCTION

The measurement scene is shown in the Figure 3. The projector is used as the light source in the simulated measurement scene. Given the optical and geometric parameters of sensors, the fringe pattern, the phase-shift parameters and the CAD model of object, the virtual phase-shift fringe pattern of the CAD model is rendered with modifying the pitch and phase offset of the sinusoidal fringe.

The projector and cameras are modeled by pinhole model and lens distortion [24], [25]. The resolution, internal and external calibration parameters of the projector and cameras refer to the physical measurement system. The world coordinate system is defined as the left camera coordinate system, and the calibration parameters are used to determine the relative position between the projector and two cameras.

The object is modeled with ideal geometry (such as standard plane, sphere, cylinder, etc.) or triangular meshes of complex surfaces. The bounding volume hierarchy (BVH)

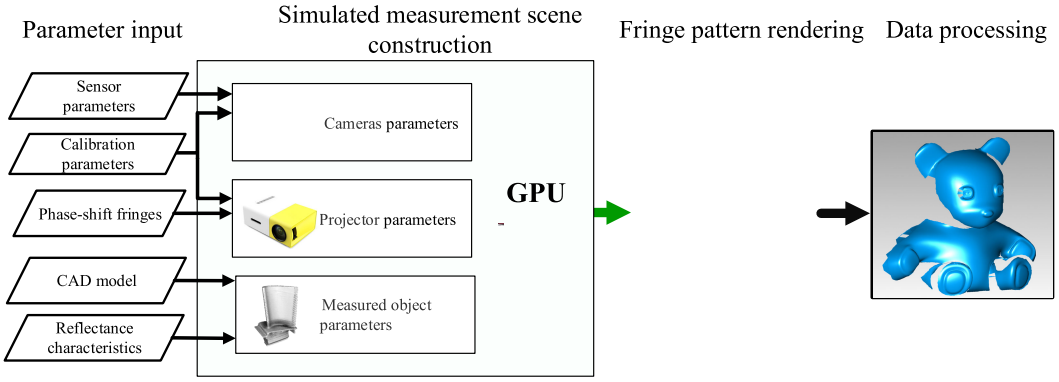

FIGURE 2. Overall scheme of simulation system.

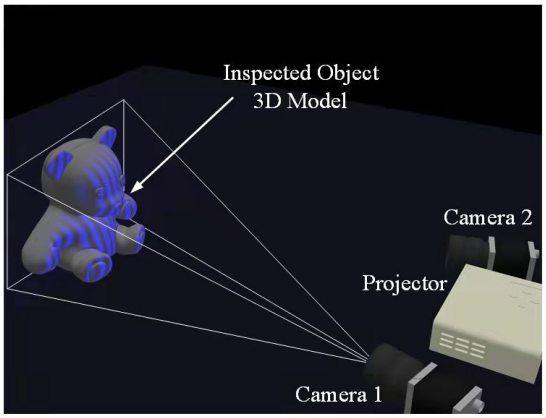

FIGURE 3. Measurement scene.

tree is constructed to accelerate ray intersection [26]. The model data and BVH tree parameters are transferred to GPU through shader storage buffer object (SSBO).

The surface reflection model is built by Phong model [27], which is a computer graphics algorithm widely used in scene rendering. The model can ensure the linear relationship between the projection light intensity and the reflected light intensity, which is consistent with the basic assumption of FPP.

B. RAY GENERATION

In this part, the ray entering the scene through pixels from the viewpoint is generated, and then the intersection between the ray and the object is solved. The multi jittered sampling is used to emit multiple rays for each pixel on the pattern [28].

Multiple jittered sampling is performed on the square area centered as each integer pixel point with half-pixel side length. As an example, taking the sampling number 16, a set of sampling points is distributed as shown in Figure 4.

The starting point and direction of ray are represented by point $\boldsymbol{r}_o$ and unit vector $\boldsymbol{r}_d$ respectively in the world coordinate system. After normalizing pixel coordinates, the parameters of ray passing through a pixel can be calculated

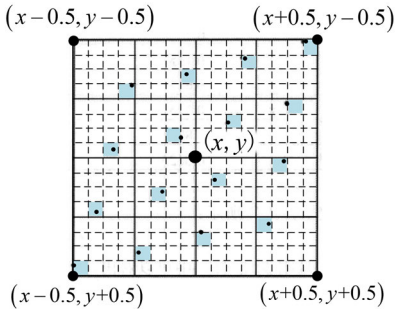

FIGURE 4. Pixel distribution generated by multiple jitter sampling.

by (1).

$$\begin{cases} \boldsymbol{r}_{\mathrm{o}} = \boldsymbol{R}^{\mathrm{T}}\left(\boldsymbol{p}_{\mathrm{Len}} - \boldsymbol{T}\right) \\ \boldsymbol{r}_{\mathrm{d}} = \boldsymbol{R}^{\mathrm{T}}\dfrac{\boldsymbol{T}_{\mathrm{d}}}{\|\boldsymbol{T}_{\mathrm{d}}\|} \\ \boldsymbol{T}_{\mathrm{d}} = \left[\dfrac{f_{\mathrm{d}}}{f_{\mathrm{l}}}x_{\mathrm{n}} - x_{\mathrm{l}}\ \dfrac{f_{\mathrm{d}}}{f_{\mathrm{l}}}y_{\mathrm{n}} - y_{\mathrm{l}}\ f_{\mathrm{d}}\right]^{\mathrm{T}} \end{cases} \tag{1}$$

where $\boldsymbol{R}$, $\boldsymbol{T}$ represent the external parameters of camera; (x_n, y_n) represents the normalized pixel coordinates; f_d and f_1 represent camera focus distance and lens focus; $\boldsymbol{P}_{Len}(x_1, y_1, 0)$ represents the sample point coordinates on lens disk.

Object instantiation is manipulated to facilitate calculation, that is, the object coordinate system and camera coordinate system are unified through transformation. After that, the intersection of ray and object is operated, as shown in the Figure 5. The specific steps are as follows

a) Generate inverse-transformed ray. According to the initial ray $(\boldsymbol{r}_o, \boldsymbol{r}_d)$, the parameters of inverse-transformed ray are obtained from (2).

$$\begin{cases} \boldsymbol{r}'_{\mathrm{o}} = \boldsymbol{T}^{-1}\boldsymbol{r}_{\mathrm{o}} \\ \boldsymbol{r}'_{\mathrm{d}} = \boldsymbol{T}^{-1}\boldsymbol{r}_{\mathrm{d}} \end{cases} \tag{2}$$

where $\boldsymbol{T}$ represents the transformation matrix. The expression of in-verse-transformed ray is shown as $(\boldsymbol{r}'_O, \boldsymbol{r}'_d)$.

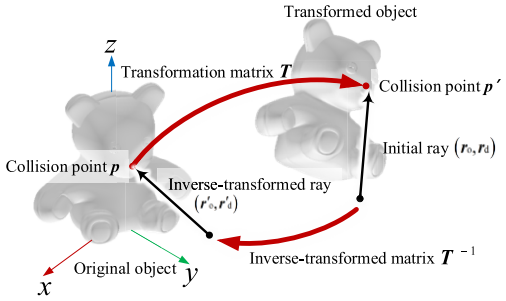

FIGURE 5. Intersection of ray and object.

b) Operate intersection of the inverse-transformed ray and the original object, their collision point $\boldsymbol{P}$ is calculated by (3).

$$\boldsymbol{p} = \boldsymbol{r}'_{\mathrm{o}} + t\boldsymbol{r}'_{\mathrm{d}} \tag{3}$$

where $\boldsymbol{t}$ is coefficient determined by the intersection.

c) Calculate normal direction $\boldsymbol{n}$ of the original object at the collision point $\boldsymbol{P}$.

d) Calculate the collision point $\boldsymbol{p}'$ between the original ray and the transformed object by (4).

$$\boldsymbol{p}' = \boldsymbol{T}\boldsymbol{p} \tag{4}$$

e) Obtain the normal direction $\boldsymbol{n}'$ of the transformed object using the normal direction $\boldsymbol{n}$ step c). $\boldsymbol{n}'$ is used for the calculation of gray value.

C. GRAY VALUE CALCULATION

Firstly, whether the intersection can be illuminated is detected according to the position of the object and the light source. If illuminated, the irradiance information of the intersection is calculated. The irradiance of pixel is obtained by integrating the light intensity, and the gray value is further obtained by quantization.

In this section, the interaction between ray and object surface is shown in Figure 6 [29]. Assuming that the incident ray intersects the object surface at point x, the incident light intensity in the positive hemisphere solid angle of $\boldsymbol{x}$ is recorded as $\boldsymbol{L}_i(\boldsymbol{x}, \boldsymbol{\omega}_i)$, and the emergent light intensity $\boldsymbol{L}_r(\boldsymbol{x}, \boldsymbol{\omega}_r)$ is obtained by the rendering equation shown in (5).

$$L_{\mathrm{r}}(\boldsymbol{x}, \boldsymbol{\omega}_{\mathrm{r}}) = \int_{\Omega^+} f_{\mathrm{r}}(\boldsymbol{\omega}_{\mathrm{i}}, \boldsymbol{x}, \boldsymbol{\omega}_{\mathrm{r}}) L_{\mathrm{i}}(\boldsymbol{x}, \boldsymbol{\omega}_{\mathrm{i}}) \cos\theta_{\mathrm{i}} \mathrm{d}\boldsymbol{\omega}_{\mathrm{i}} \tag{5}$$

where, $\boldsymbol{\Omega}^+$ represents the positive hemisphere solid angle; $\boldsymbol{\omega_i}$ represents incident direction; $f_r(\boldsymbol{\omega_i}, \boldsymbol{x}, \boldsymbol{\omega_r})$ represents bidirectional reflectance distribution function (BRDF).

Based on the principle of Monte Carlo integration [28], the light intensity reflected by the intersection area between multiple rays and the object surface is integrated. The light intensity is related to the position of projection point, fringe pitch and phase shift parameters.

The schematic diagram of single ray tracing is shown in Figure 7. Assuming that a ray intersects the object surface at

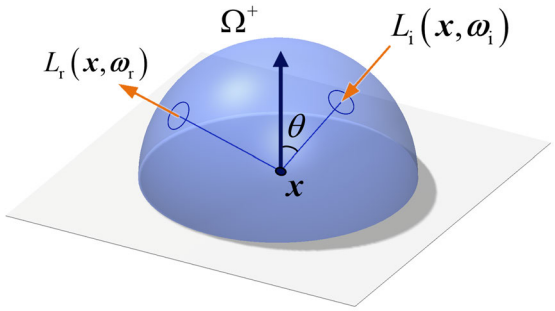

FIGURE 6. Schematic diagram of interaction between ray and object surface.

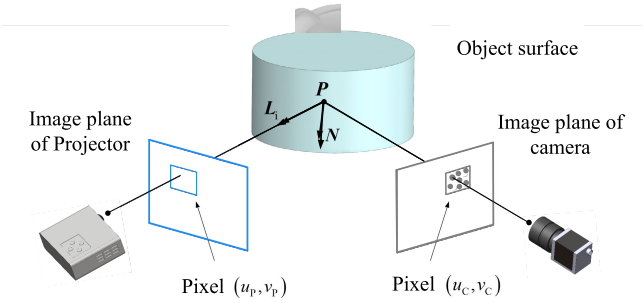

FIGURE 7. Schematic diagram of single ray tracing.

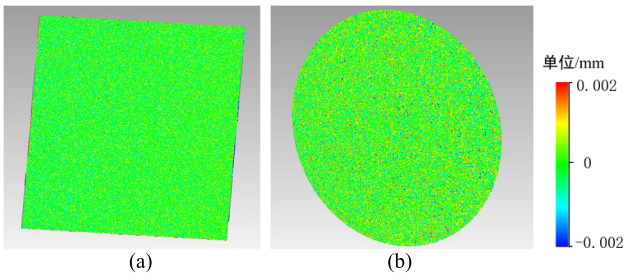

FIGURE 8. Fitting error distribution: (a) Fitting error distribution of plane; (b) Fitting error distribution of sphere.

point $\boldsymbol{P}$, the contribution of the ray to the light intensity is expressed as $I_k(i,j)$ by (6).

$$I_k(i,j) = \frac{\rho_d}{\pi} \cdot l_p \cdot (I_a + I_b \cos\Phi_k) \cdot (\boldsymbol{N} \cdot \boldsymbol{L}_i) \cdot V(\boldsymbol{P}) \tag{6}$$

$V(\boldsymbol{P})$ indicates the visibility of point $\boldsymbol{P}$. If $\boldsymbol{P}$ is visible, $V(\boldsymbol{P}) = 1$, otherwise $V(\boldsymbol{P}) = 0$. $\rho_d, \boldsymbol{N}$ are reflectivity and normal vector of object surface respectively. $\boldsymbol{L}_i$ represents the direction vector of incident ray. $I_a, I_b, \boldsymbol{\Phi}_k$ represent the direct component, modulation and phase offset of sinusoidal fringe respectively.

The total light intensity $I(i,j)$ is obtained by (7), which is an approximate solution to (5).

$$I(i,j) = \sum_{k=1}^{K} w_k I_k(i,j) \tag{7}$$

where, $w_k(k = 1, \ldots, j)$ is the weight of rays.

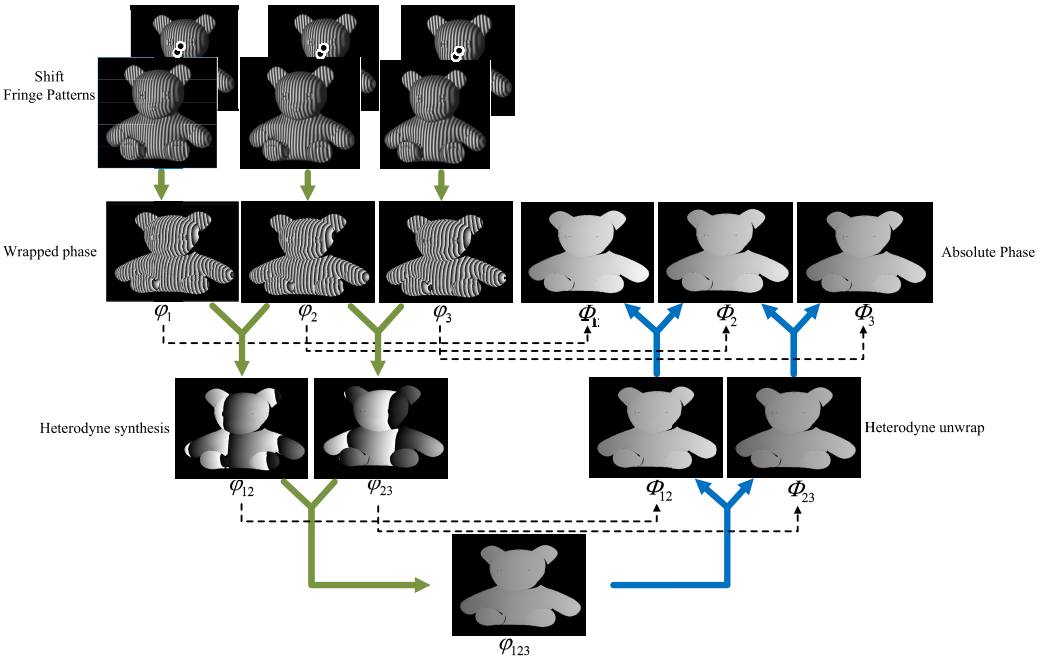

FIGURE 9. Fringe patterns and phase retrieving results.

IV. EXPERIMENT VERIFICATION

In this section, the parameters of the simulation system are given with reference to the physical measurement system, besides, the principle experiment and comparative experiment are designed to illustrate the effectiveness of simulation system. In the principle experiment, the measurement accuracy and efficiency of the simulation system are proved by the simulation measurement of the standard plane, sphere and bear model. In the comparative experiment, the simulation measurement of the standard sphere is compared with the physical measurement results to verify the reproducibility of the simulation system to the physical system.

A. PARAMETERS OF SIMULATION SYSTEM

The parameters of simulation system are set with reference to the physical measurement system, as shown in Table 1. The operating environment of the simulation system is shown in Table 2.

The camera calibration based on 2D plane target and the ''camera-projector'' calibration based on phase shift are implemented [30], [31]. The calibration results of internal and external parameters are shown in Table 3 and Table 4.

TABLE 1. Parameters of the Simulation System.

Parameters	Value	Parameters	Value
Camera resolution	1440×1080 pixel	Aperture number F	8
Camera exposure time	30ms	Fringe pitches	13、14、15 pixel
Camera focal length	10mm	Phase shift steps	4
Pixel size	3.45μm	Sample count per pixel	1024
Projector resolution	1280×720 pixel	Light intensity of projector	40

TABLE 2. Operating Environment of Simulation System.

Operating system	CPU	RAM	GPU
Windows 10	Intel(R) Core (TM) i7-10750H, 2.60GHz	32.0 GB	NVIDIA Quadro P620 (4095MB)

B. PRINCIPLE EXPERIMENT OF SIMULATION SYSYTEM

Firstly, the ideal plane and sphere are measured by simulation system to verify the system accuracy. The diameter of the ideal sphere is 10mm and the center coordinate is (0,0,250). The intersection of ray and sphere is obtained by analytical method. The rendering time of single fringe pattern is 0.18s, and the whole simulated measurement process takes 2.2s.

The simulated data of plane and sphere are fitted, and the error distribution is shown in the Figure 8. Figure 8(a) expresses fitting error distribution of plane, with the root mean square error (RMSE) value of 0.0013mm. Figure 8(b) expresses fitting error distribution of sphere, with the RMSE value of 0.0016mm. Gray noise is not introduced into the simulation process.

TABLE 3. Calibration Results of Internal Parameters.

Internal Parameters	α_x	α_y	u_0	v_0	k_1	k_2	p_1	p_2
Left camera	2359.53	2359.09	734.47	578.34	-0.1251	0.1620	0.0003	-0.0004
Right camera	2360.53	2359.81	736.99	580.87	-0.1170	0.1249	0	-0.0002
Projector	1700.15	1701.22	627.73	406.54	0.1328	-0.3361	-0.0006	-0.0001

TABLE 4. Calibration Results of External Parameters.

External Parameters	θ_x	θ_y	θ_z	t_1	t_2	t_3
Left camera - right camera	-0.0086	0.7078	0.0058	-189.5009	-1.1664	66.0589
Left camera- projector	-0.0099	0.3754	0.0276	-94.5914	-0.1889	12.4706

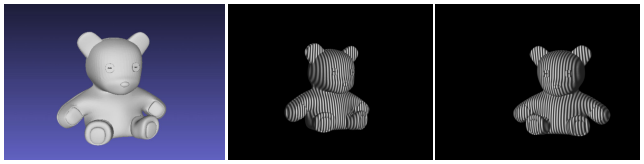

FIGURE 10. Model and fringe patterns: (a) Bear model; (b) Fringe pattern rendered by left camera; (c) Fringe pattern rendered by right camera.

FIGURE 11. Wrapped phase of the left pattern.

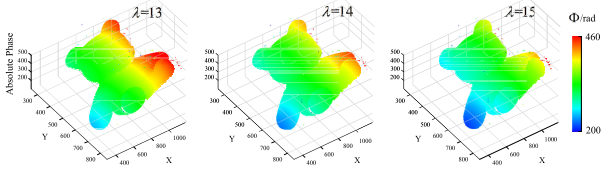

FIGURE 12. Unwrapped phase of the left pattern.

Taking the bear model as measured object, the effectiveness of the simulation system for complex surface is verified. The fringe patterns and phase retrieving results of the bear are shown in Figure 9. Figure 10 (a), (b) and (c) respectively show the bear model, simulated fringe pattern rendered by left camera and right camera. The fringe pitch corresponding to Figure 10 (b) and (c) is 15 pixels and the phase shift is 0.

The wrapped phase and unwrapped phase of the left pattern are shown in Figure 11 and Figure 12 respectively.

The reconstruction of bear model is shown in Figure 13. The number of triangular meshes is 85504, the rendering time of single fringe pattern is 3.8s, and the whole simulated measurement takes 45.8s.

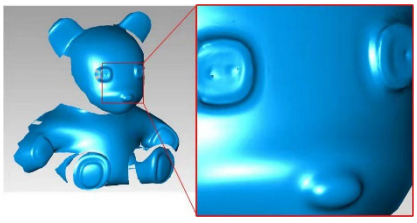

FIGURE 13. Reconstruction of bear model.

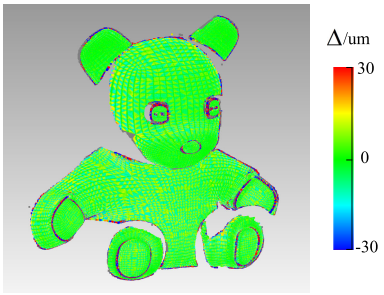

FIGURE 14. Deviation distribution of registered point cloud and CAD model.

The reconstructed point cloud is registered with the CAD model by iterative closest point (ICP) algorithm [32], and the distance from each measurement point to the model is calculated to obtain the deviation distribution as shown in Figure 14. The RMSE of registered point cloud and CAD model is 0.015mm.

C. COMPARATIVE EXPERIMENT BETWEEN SIMULATION SYSTEM AND PHYSICAL SYSTEM

Taking a standard sphere as the measured object, the experimental scheme is shown in Figure 15. Firstly, the physical system is used to measure the form and spatial position of the sphere. On this basis, a virtual measured object is constructed, and the form and spatial position of the virtual sphere are measured by the simulation system. By comparing the measurement results of the pairwise

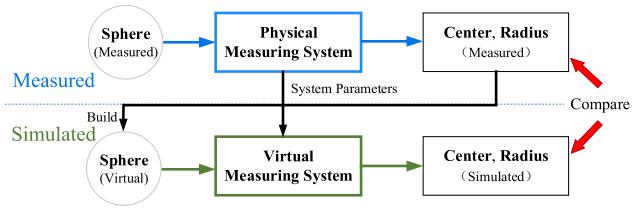

FIGURE 15. Scheme of comparative experiment.

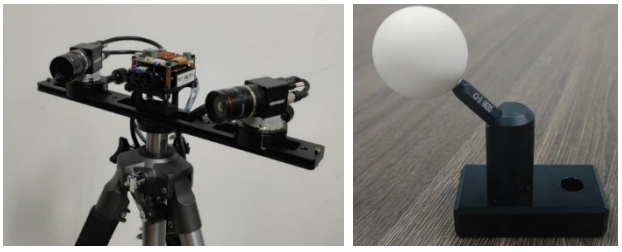

FIGURE 16. Physical measurement system and measured object.

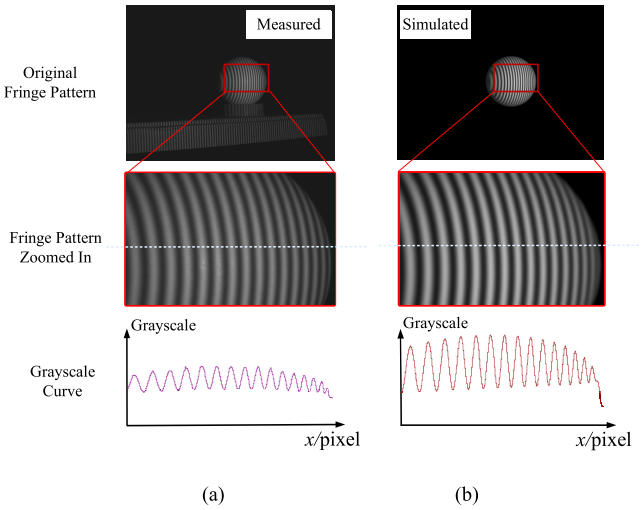

FIGURE 17. Comparison results of fringe pattern: (a) Captured fringe pattern of physical system; (b) Rendered fringe pattern of simulation system.

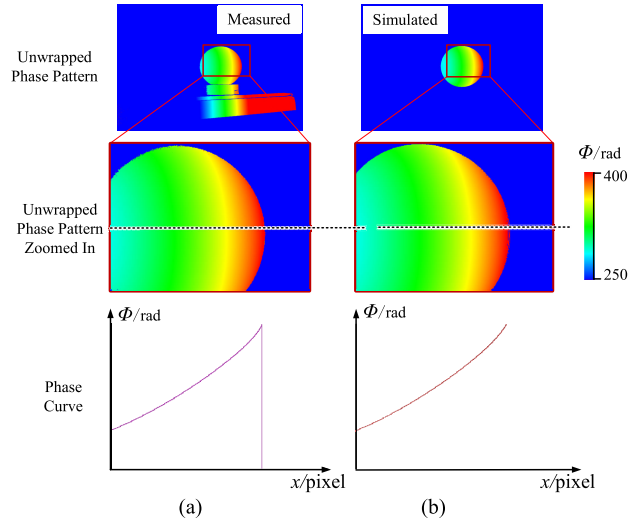

FIGURE 18. Comparison results of phase distribution: (a) physical measured unwrapped phase pattern; (b) simulated unwrapped phase map.

systems, the reproducibility of the simulation system is verified.

The physical measurement system and measured object are shown in Figure 16. The physical system consists of one digital projector (DLP 3010), two monochrome cameras (MV-CA016-10UM) and auxiliary cables. The standard sphere with nominal diameter of 38.106mm is taken as the measured object. The roundness of the standard sphere is 0.0035mm.

To compare the measurement process, the fringe pattern with fringe pitch of 15 pixels and phase shift value of 0 is selected. Figure 17 shows the comparison results and the grayscale curve of 500th-row pixels. Figure 17(a) illustrates the captured fringe pattern of physical system, while (b) is rendered fringe pattern of simulation system.

Figure 18 shows the comparison results of phase distribution and the phase curve of 500th-row pixels. Figure 18(a) and (b) show the physical measured and simulated unwrapped phase map respectively.

Table 5 shows the measurement results of the sphere, in which the center coordinates (cen_x, cen_y, cen_z) and radius r are determined according to the least square method.

V. DISCUSSION

In the principle experiment, the fitting error distribution of plane and sphere are random. The RMSE of fitting error is less than $2\mu m$. The smaller the RMSE, the higher the accuracy of the simulation system. The reason of fitting error is that the rendered fringe patterns are quantized by 8 bits of gray scale. By increasing the bit depth, such as 10 bits or 12 bits, the phase retrieve accuracy can be significantly improved, so as to reduce the fitting error.

From the reconstruction results of the bear model, the deviation between the registered point cloud and the CAD model is mostly within $10\mu m$. A few points with large deviation are concentrated at the edge of the measurement volume and the area with drastic curvature change. The reasons for this result are as follows. At the edge of the measurement volume, the angle between the surface normal direction and the light direction is large, resulting in the dark fringe pattern, which reduces the modulation of sinusoidal fringe and increases the random phase error. Besides, fringe aliasing is easy to occur in the region where the curvature changes sharply, resulting in the mismatch of corresponding points, which leads to the systematic phase error.

The rendering of single fringe pattern takes several seconds, and the rendering time depends on the amount of calculation and the floating-point computing power of GPU. The parameters that affect the amount of calculation include the count of sampling points of single pixel, the resolution

TABLE 5. Measurement results of sphere (/mm).

Parameters	physical measured results	Simulation results
cen_x	6.567	6.564
cen_y	-5.497	-5.499
cen_z	270.634	270.626
r	19.065	19.061
RMSE	0.013	0.008

of the cameras and the complexity of measured object. The rendering time of triangular meshes is significantly longer than that of standard geometries.

The measured and simulated results in Figure 17 show that the grayscale variation of fringe patterns is consistent, but the gray value of the same pixel is different. The reason is that, a coefficient in the simulation system simplifies the photoelectric conversion process of the physical system. The gray value can be closer by changing the coefficient. Figure 18 shows that the phase distribution of the physical system and the simulation system is basically same, and the average phase deviation is less than 0.1%. As can be seen from Table 5, the center and radius obtained by physical measurement and simulation are consistent. The RMSE of fitting result from measured data is large, which is due to gray noise and nonuniform surface reflectivity.

In the comparative experiment, there is a slight deviation between the measurement results of the simulation system and the physical system, which is mainly due to the following reasons. On the one hand, the input parameters of the simulation system originate from the measurement results of the physical system, which are limited with the calibration accuracy; on the other hand, the measured model is simplified in the simulation system, without considering the spectral response, surface roughness and dispersion.

VI. CONCLUSION

Aiming at the problem of accurate simulation of image acquisition within fringe projection method, a 3D measurement virtual system using ray tracing is developed. The accuracy and efficiency of this system is illustrated by principle experiments of standard gauges and complex surface workpieces. The reproducibility to the physical system is verified by the comparative experiment.

The measurement simulation system of FPP based on ray tracing has the following advantages. Low cost and high efficiency are achieved by using computer simulation instead of physical system. The influence of various parameters on the measurement error can be studied by configuring different sensors and measured objects conven-iently and accurately.

REFERENCES

[1] L. Yu, W. Zhang, and H. Luo, "Measurement technique of complex curved-profile based on fringe projection profilometry," *Metrology Meas. Technol.*, vol. 38, no. 3, pp. 82–90, Aug. 2018.

[2] A. Weckenmann, W. Hartmann, and J. Weickmann, "Model and simulation of fringe projection measurements as part of an assistance system for multi-component fringe projection sensors," *Proc. SPIE*, vol. 7102, no. 4, pp. 317–347, 2008.

[3] E. Cui, "Research on key techniques of high-precision binocular visual measurement system," Ph.D. dissertation, Changchun Inst. Optics, Univ. Chinese Acad. Sci., Changchun, China, Jun. 2018.

[4] C. Bernal, B. de Agustina, M. M. Marín, and A. M. Camacho, "Accuracy analysis of fringe projection systems based on blue light technology," *Key Eng. Mater.*, vol. 615, pp. 9–14, Jun. 2014.

[5] Z. Zhang and D. Jie, "Error analysis of a 3D imaging system based on fringe projection technique," *Proc. SPIE*, vol. 9042, Dec. 2013, Art. no. 2034337, doi: 10.1117/12.2034337.

[6] X. Bian, X. Su, and W. Chen, "Analysis on 3D object measurement based on fringe projection," *Optik*, vol. 122, no. 6, pp. 471–474, Mar. 2011.

[7] T. Böttner and M. Köstner, *The Virtual Fringe Projection System (VFPS) and Neural Networks*, W. Osten, Eds. Berlin, Germany: Springer, 2005, doi: 10.1007/3-540-29303-5_22.

[8] J. Weickmann, A. Weckenmann, and P. F. Brenner, "Automatic, task-sensitive and simulation-based optimization of fringe projection measurements," *Key Eng. Mater.*, vol. 437, pp. 439–443, May 2010.

[9] A. Weckenmann, W. Hartmann, and J. Weickmann, "Multi-component fringe projection sensors: Assistance system for short and robust inspection processes," in *Proc. NCSL Int. Workshop Symp.*, 2008, pp. 43–49.

[10] T. Peng, "Algorithms and models for 3-D shape measurement using digital fringe projections," Ph.D. dissertation, Dept. Mech. Eng., Inst. Syst. Res., Univ. Maryland, College Park, MD, USA, 2006.

[11] Y. Chen and W. Li, "A novel algorithm for fringe projection profilometry," *Opt. Instrum.*, vol. 39, no. 4, pp. 1–6, 2017.

[12] W. Li, S. Fang, and S. Duan, "Accurate and efficient algorithm for simulation of fringe projection system," *Optik Int. J. Light Electron Opt.*, vol. 124, no. 18, pp. 3542–3548, Sep. 2013.

[13] K. Haskamp, M. Kästner, and C. Ohrt, and E. Reithmeier, "Estimation of measurement uncertainties using virtual fringe projection technique," *Appl. Opt.*, vol. 51, pp. 1516–1520, Apr. 2012.

[14] P. Lutzke, S. Heist, P. Kühmstedt, R. Kowarschik, and G. Notni, "Monte Carlo simulation of three-dimensional measurements of translucent objects," *Opt. Eng.*, vol. 54, no. 8, Aug. 2015, Art. no. 084111.

[15] H. Zhao, L. Xu, S. Shi, H. Jiang, and D. Chen, "A high throughput integrated hyperspectral imaging and 3D measurement system," *Sensors*, vol. 18, no. 4, p. 1068, Apr. 2018.

[16] S. Irgenfried, S. Bergmann, M. Mohammadikaji, J. Beyerer, C. Dachsbacher, and H. Wörn, "Image formation simulation for computer-aided inspection planning of machine vision systems," in *Proc. SPIE*, Jun. 2017, p. 10334, doi: 10.1117/12.2269166.

[17] M. Mohammadikaji, S. Bergmann, J. Beyerer, J. Burke, and C. Dachsbacher, "Sensor-realistic simulations for evaluation and planning of optical measurement systems with an application to laser triangulation," *IEEE Sensors J.*, vol. 20, no. 10, pp. 5336–5349, May 2020, doi: 10.1109/JSEN.2020.2971683.

[18] T. Becker, M. Özkul, and U. Stilla, "Simulation of close-range photogrammetric systems for industrial surface inspection," *Int. Arch. Photogramm., Remote Sens. Spatial Inf. Sci.*, vol. 38, pp. 179–183, Apr. 2011.

[19] A. Mezhenin, V. Polyakov, and A. Prishhepa, "Using virtual scenes for comparison of photogrammetry software," in *Proc. Int. Symp. Comput. Sci., Digit. Economy Intell. Syst.* Cham, Switzerland: Springer, 2020, pp. 57–65.

[20] D. B. Gajic, S. Mihic, D. Dragan, V. Petrovic, and Z. Anisic, "Simulation of photogrammetry-based 3D data acquisition," *Int. J. Simul. Model.*, vol. 18, no. 1, pp. 59–71, Mar. 2019.

[21] P. Shirley, R. K. Morley, and K. Morley, *Realistic Ray Tracing*, 2nd ed. Boca Raton, FL, USA: CRC Press, 2003.

[22] E. Haines and T. Akenine-Möller, *Ray Tracing Gems: High-Quality and Real-Time Rendering With DXR and Other APIs*. Berkeley, CA, USA: Apress, 2019, doi: 10.1007/978-1-4842-4427-2.

[23] H. Jiang, H. Zhao, and X. Li, "High dynamic range fringe acquisition: A novel 3-D scanning technique for high-reflective surfaces," *Opt. Lasers Eng.*, vol. 50, no. 10, pp. 1484–1493, Oct. 2012.

[24] S. Gai, F. Da, and X. Dai, "A novel dual-camera calibration method for 3D optical measurement," *Opt. Lasers Eng.*, vol. 104, pp. 126–134, May 2018.

[25] R. Chen, J. Xu, H. Chen, J. Su, Z. Zhang, and K. Chen, "Accurate calibration method for camera and projector in fringe patterns measurement system," *Appl. Opt.*, vol. 55, no. 16, pp. 4293–4300, Jun. 2016, doi: 10.1364/AO.55.004293.
[26] M. Vinkler, V. Havran, and J. Sochor, "Visibility driven BVH build up algorithm for ray tracing," *Comput. Graph.*, vol. 36, no. 4, pp. 283–296, Jun. 2012, doi: 10.1016/J.CAG.2012.02.013.
[27] M. Pharr, W. Jakob, and G. Humphreys, *Physically Based Rendering*, vol. 13, 2nd ed. San Mateo, CA, USA: Morgan Kaufmann, 2010, pp. 97–107, doi: 10.1016/C2013-0-15557-2.
[28] N. Hofmann and A. Evans, "Efficient unbiased volume path tracing on the GPU," in *Ray Tracing Gems II*. Berkeley, CA, USA: Apress, 2021, pp. 699–711.
[29] M.-G. Retzlaff, J. Hanika, J. Beyerer, and C. Dachsbacher, "Physically based computer graphics for realistic image formation to simulate optical measurement systems," *J. Sensors Sensor Syst.*, vol. 6, no. 1, pp. 171–184, May 2017.
[30] Z. Zhang, "A flexible new technique for camera calibration," *IEEE Trans. Pattern Anal. Mach. Intell.*, vol. 22, no. 11, pp. 1330–1334, Nov. 2000, doi: 10.1109/34.888718.
[31] P. S. Huang, "Novel method for structured light system calibration," *Opt. Eng.*, vol. 45, no. 8, Aug. 2006, Art. no. 083601.
[32] X. Cheng, Z. Li, K. Zhong, and Y. Shi, "An automatic and robust point cloud registration framework based on view-invariant local feature descriptors and transformation consistency verification," *Opt. Lasers Eng.*, vol. 98, pp. 37–45, Nov. 2017, doi: 10.1016/J.OPTLASENG.2017.05.011.

QIUSHUANG ZHANG received the B.S. degree in mechanical manufacturing and automation from North China Electric Power University, Hebei, in 2015, and the Ph.D. degree in mechanical engineering from the Beijing Institute of Technology, Beijing, China, in 2020.

Since 2020, she has been a Special Associate Professor with the Intelligent Manufacturing Department, Qingdao University of Science and Technology, Qingdao. She is the author of more than ten articles and more than five inventions. She is engaged in research in the field of precision assembly, including error modeling and evaluation, performance prediction and optimization, digital twinning, and 3D measurement.

Dr. Zhang is a member of the Chinese Society for Optical Engineering.

MINGYI XING received the B.S. and M.S. degrees in instrument science and technology from Beihang University, Beijing, in 2021.

Since 2021, he has been a Software Engineer with the Ultrasound Research and Development Department, Hisense Medical Equipment Company Ltd., Qingdao. His research interests include structured light, deep learning, and 3D measurement.

Mr. Xing is a member of the Chinese Society for Optical Engineering.

HONGBIN LI received the B.S. degree in mechanical design, manufacturing, and automation from the Wuhan University of Technology, in 2013, and the M.S. and Ph.D. degrees in mechanical engineering from Tianjin University, Tianjin, in 2020.

Since 2020, he has been a Special Associate Professor with the Intelligent Manufacturing Department, Qingdao University of Science and Technology, Qingdao. His research interests include additive manufacturing and intelligent equipment design.

XU LI received the B.S. degree in mechanical design manufacturing and automation from Yangtze University, Hubei, China, in 2022. He is currently pursuing the M.S. degree in mechanical engineering with the Qingdao University of Science and Technology, Qingdao, China.

His research interests include machine learning and 3D measurement technology.

Mr. Li was awarded the China National Scholarship.

TINGLI WANG received the B.S. degree in materials science and engineering from the China University of Petroleum, in 2004, and the M.S. degree in material processing engineering from the Dalian University of Technology, in 2017.

From 2007 to 2019, he was a Senior Engineer with Dalian Bingshan Metal Technology Company Ltd. Since 2020, he has been an Associate Professor with the Intelligent Manufacturing Department, Qingdao University of Science and Technology, Qingdao. His research interest includes additive manufacturing equipment and related measurement technologies.